Journal of
Applied Crystallography

ISSN 0021-8898

Received 7 May 2013
Accepted 28 August 2013

Obtaining the structure factors for an epitaxial film using Cu X-ray radiation

P. Wadley,[a,b] A. Crespi,[c] J. Gázquez,[c] M.A. Roldán,[d,e] P. García,[f] V. Novak,[a] R. Campion,[b] T. Jungwirth,[a,b] C. Rinaldi,[g] X. Martí,[a,h,i]* V. Holy,[h] C. Frontera[c] and J. Rius[c]

[a]Institute of Physics ASCR, v.v.i. Cukrovarnická, Prague, Czech Republic, [b]School of Physics and Astronomy, University of Nottingham, UK, [c]Institut de Ciència de Materials de Barcelona, ICMAB-CSIC, Bellaterra, Spain, [d]Departamento de Física Aplicada III, Universidad Complutense de Madrid, Madrid, Spain, [e]Materials Science and Technology Division, Oak Ridge National Laboratory, USA, [f]Centre Investigació Nanociència Nanotecnologia, CIN2, Bellaterra, Spain, [g]LNESS – Dipartimento di Fisica, Politecnico di Milano, Como, Italy, [h]Faculty of Mathematics and Physics, Charles University in Prague, Czech Republic, and [i]Department of Physics, University of California, Berkeley, USA. Correspondence e-mail: xaviermarti@berkeley.edu

Determining atomic positions in thin films by X-ray diffraction is, at present, a task reserved for synchrotron facilities. Here an experimental method is presented which enables the determination of the structure factor amplitudes of thin films using laboratory-based equipment (Cu $K\alpha$ radiation). This method was tested using an epitaxial 130 nm film of CuMnAs grown on top of a GaAs substrate, which unlike the orthorhombic bulk phase forms a crystal structure with tetragonal symmetry. From the set of structure factor moduli obtained by applying this method, the solution and refinement of the crystal structure of the film has been possible. The results are supported by consistent high-resolution scanning transmission electron microscopy and stoichiometry analyses.

1. Introduction

Subtle modifications of the unit-cell topology can lead to dramatic changes in the magnetic, dielectric, optic, chemical *etc.* properties of materials. From this perspective, one of the major advantages of thin-film growth is the ability to fine tune lattice parameters, bond angles and distances in the unit cell to obtain enhanced or completely new functionalities. For bulk single crystals and powder samples, diffraction methods are perfectly suited for structural refinement and can be performed with unrivalled accuracy. However, in the case of epitaxial thin films, unravelling the fine structural details governing their functionalities is a task reserved for synchrotron radiation facilities (May *et al.*, 2010). Meanwhile, the majority of laboratory analyses are restricted to the accurate determination of the lattice parameters and do not provide critical structural information such as bonding angles or bond lengths. The increasing interest in thin-film materials provides a great incentive for quick methodologies to unravel structural details, particularly for rapid feedback during material growth, using routinely available X-ray diffraction setups. Such analysis techniques are still a developing field (Ferrari & Lutterotti, 1994).

To obtain a complete description of the unit cell, intensity data of as many diffraction peaks as possible (including systematic extinctions) must be obtained. A conventional high-resolution diffraction experiment can accurately determine the lattice parameters from a reduced set of reflections, but it is unable to collect an exhaustive list of relative peak intensities in a reasonable time frame. Moreover, the high-resolution coplanar setup for thin epilayers obscures several reflections because of the shadowing effect of the sample holder. To overcome these issues, two-dimensional plate detectors placed at short distances from the thin-film sample are a time-efficient way to collect the integrated intensities, but at the cost of lowering the resolution. By combining the data from both experimental setups, it is possible to perform a complete structural study of the thin layer in a precise and time-efficient manner.

In this article, we present explicit formulae to derive the moduli of the structure factors of an epitaxial thin film from a set of relative intensities obtained by two-dimensional detector measurements. To demonstrate this methodology, we have selected a thin film (130 nm) grown by molecular beam epitaxy that crystallizes in a tetragonal phase while the bulk stable phase is orthorhombic. After determining the lattice parameters by high-resolution measurements, we have collected the intensities using a plate detector, and then integrated and corrected them to finally obtain the set of structure factor moduli. These have been subsequently phased by δ recycling direct methods and the resulting structural model has been successfully refined. Of particular relevance is the fact that the diffraction experiment only requires Cu $K\alpha$ radiation sources. The thickness of the sample (130 nm, which represents more than 200 unit cells) is large enough to treat

data as in a bulk case, *i.e.* it has been assumed that the intensity is predominantly concentrated forming Bragg peaks with the truncation rods playing no significant role. This means that it is the average structure of the whole film that is determined, so that variations of the structure across the film have not been considered. This study provides a basis for the performance of accurate structural studies in thin-film samples using basic laboratory equipment, without the need of measurements at large facilities (with the inherent time delays).

The article is organized as follows: In §2 we describe the sample preparation, the experimental setup and the measurement procedure. The corrections for integrating the peak intensities are summarized in §3 (and derived in Appendix *A*). The application of δ recycling and the refinement of the unit-cell contents are discussed in §4. §5 summarizes the results and presents consistent high-resolution scanning transmission electron microscopy (HR-STEM) and stoichiometry analyses on pieces of the same sample.

2. Sample preparation, experimental setup and measuring procedure

The CuMnAs thin layer that we used to validate this study was grown by molecular beam epitaxy on a GaAs(001) substrate. Details of the sample preparation can be found elsewhere (Wadley *et al.*, 2013). A 5 × 2 mm sample was cut from the original wafer for use in the present study. The thickness of the CuMnAs layer is 130 (3) nm according to X-ray reflectivity (not shown). From the reflection high-energy electron diffraction (RHEED) patterns collected during the growth, the sample is epitaxial and has in-plane square symmetry (Wadley *et al.*, 2013), at odds with the expectations of the orthorhombic phase of CuMnAs (Mundelein & Schuster, 1991; Mašek *et al.*, 2012). This discrepancy provided the motivation for a detailed crystal structure analysis.

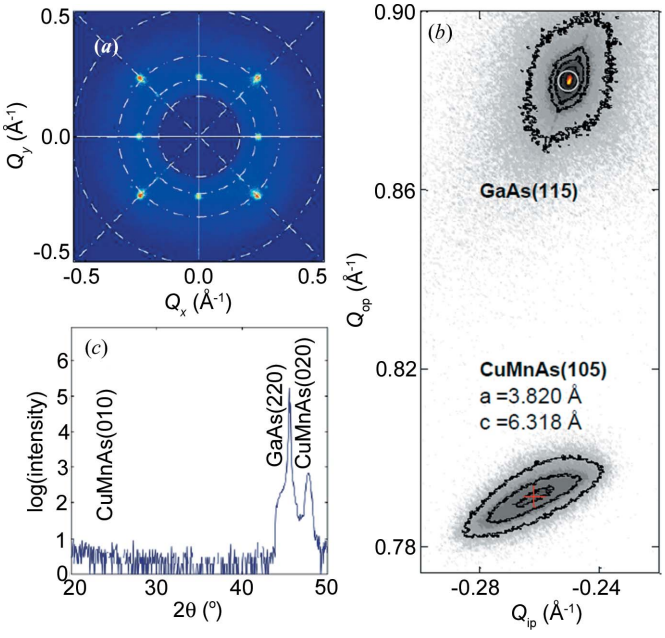

Figure 1
(*a*) In-plane projection of the reciprocal space collected around the GaAs(202) reflection, evidencing the in-plane fourfold symmetry of the CuMnAs thin film corresponding to [100]GaAs(001)/[110]CuMnAs(001). (*b*) Coplanar reciprocal space map around the GaAs(115) reflection. In-plane and out-of-plane parameters extracted from the coplanar reciprocal space map. (*c*) In-plane diffraction scan along the [110]GaAs direction revealing CuMnAs(020) and evidencing the absence of CuMnAs(010).

Table 1
Raw integrated intensity I^{M} and structure factors for each *hkl* reflection located at the angular position 2θ, ψ and ω (given in degrees).

F_o is the corresponding observed structure factor (after applying to I the corrections detailed in Appendix *A*), and F_c is the calculated structure factor (from the refinement).

h	*k*	l	2θ	ψ	ω	I^{M}	F_o^2	F_c^2
0	0	1	16.00	0.00	0.50	43.40	1.87	1.79
0	1	1	27.38	13.69	66.00	27.56	1.34	1.37
1	1	1	36.14	67.00	18.15	102.31	8.64	8.87
0	2	1	50.10	73.22	25.05	3.47	0.46	0.65
1	2	1	55.99	78.00	27.99	7.54	0.97	0.85
2	2	1	71.34	77.97	35.88	0.74	0.16	0.26
0	3	1	76.67	80.64	38.33	3.85	0.75	0.58
1	3	1	80.94	79.21	40.73	9.82	2.39	1.78
2	3	1	94.95	80.51	48.50	2.05	0.52	0.40
0	0	2	28.00	0.00	6.50	14.05	1.88	1.73
0	1	2	37.03	39.66	18.51	7.06	0.84	0.88
1	1	2	44.11	52.00	22.13	124.70	21.65	21.46
0	2	2	56.51	60.00	28.25	2.68	0.72	1.05
1	2	2	61.69	61.66	30.99	1.01	0.32	0.35
2	2	2	76.68	67.90	38.55	1.17	0.48	0.74
0	3	2	81.90	68.10	40.95	0.24	0.11	0.16
1	3	2	86.11	70.50	43.32	16.61	7.33	5.54
0	0	3	43.00	0.00	14.00	44.78	15.02	14.10
0	1	3	49.55	31.00	24.70	18.85	3.82	3.90
1	1	3	55.35	38.01	27.74	0.47	0.14	0.06
0	2	3	66.28	48.00	33.14	13.88	6.08	6.34
1	2	3	71.05	51.02	35.66	4.35	2.17	2.19
2	2	3	85.35	57.38	42.89	5.82	3.63	3.15
0	3	3	90.49	58.90	45.24	2.19	1.40	1.31
1	3	3	94.68	60.23	47.60	0.60	0.38	0.05
0	0	4	58.50	0.00	21.75	10.40	6.96	6.58
0	1	4	63.92	22.52	31.96	0.50	0.14	0.10
1	1	4	68.93	30.38	34.53	0.66	0.28	0.00
0	2	4	78.87	39.66	39.43	4.86	2.92	3.48
1	2	4	83.36	42.83	41.82	0.09	0.06	0.04
2	2	4	97.36	49.54	48.90	2.52	1.86	1.95
0	1	5	80.18	18.35	40.09	8.71	3.26	3.48
1	1	5	84.80	25.13	42.47	3.90	2.03	2.81
0	1	6	99.12	15.45	49.56	0.35	0.13	0.24

High-resolution X-ray diffraction experiments were performed using a Panalytical X'Pert material research diffractometer, equipped with an X-ray mirror and a Bartels monochromator on the incident beam side and a PixCel linear detector on the diffracted beam side. The relative intensities were collected on a Bruker D8 diffractometer equipped with an X-ray mirror, a double pinhole on the incident beam side and a general area detector diffraction system (GADDS) on the diffracted beam side, located 14 cm from the sample. Both setups used Cu anode tubes. By means of a Cu mask we restricted the active area of the detector to 3 cm in diameter to avoid the simultaneous counting of two or more very intense substrate peaks.

After placing the sample, we first identified the substrate azimuthal orientation by performing a 360° φ scan of a known

reflection. Detailed inspection of the angular (Ψ, $2\theta/\omega$ and φ) dependence of a few peaks stemming from the thin layer (those not attributed to the substrate) allowed the prediction of the remaining film reflections. [In this article we follow the same angle and sign conventions as He (2009)]. Inspection of the diffraction peaks suggested a tetragonal symmetry (Fig. 1*a*), consistent with the RHEED patterns collected during growth. We explored in detail one of the reflections using the high-resolution setup to determine the corresponding lattice parameters (Fig. 1*b*), and we obtained the values a = 3.820 (5), c = 6.318 (5) Å. Details of the extraction of the integrated intensities for each reflection are addressed in the next section.

The set of observed intensities is listed in Table 1. Systematic absences follow the condition $l = 0$ ($hk0$ with $h + k$ odd and $0k0$ with k odd). This extinction rule [notice, for instance, the extinction of 010 in Fig. 1(*c*)] is consistent with the *P*4/*nmm* space group (No. 129). Very recent crystal growth experiments have demonstrated that bulk CuMnAs can also be stabilized in the tetragonal phase with space group and lattice parameters very similar to our findings in analogous thin epilayers (Nateprov *et al.*, 2011)

3. Correction of peaks intensities

We collected the intensity for a given reflection by either rocking the sample or performing azimuthal rotations. We forced the diffraction peaks to completely cross the Ewald sphere (detector surface) in two types of scans, ω and φ scans. We employed the former for hkl reflections with $h = k = 0$ (and $l \neq 0$) and the latter for reflections with h and/or $k \neq 0$ (and $l \neq 0$). Scans were extended for 10° around the central position of the scanning motor over a period of 1–2 h (inversely proportional to the estimated intensity of the film's reflections).

The resulting images contain peaks that were subsequently fitted by means of a two-dimensional Gaussian function. The prefactor of the Gaussian (normalized to the counting time) is taken as the raw integrated intensity I_{hkl}. In all collected images the substrate peaks are completely, or nearly completely, suppressed by using the aforementioned mask, which has a 3 cm diameter aperture. The background contribution was calculated by fitting a surface with polynomials of first order to the surrounding region of the film. Errors caused by sample misalignment were quantified by comparing the integrated intensities of four symmetry-equivalent reflections of GaAs(202). We found an 11% intensity spread, and this value has been considered as the uncertainty for the computations.

The integrated intensities ($I^{\rm M}_{hkl}$) corresponding to the most intense collected reflections are listed in Table 1. To obtain the square of the structure factor moduli F^2_{hkl} for thin films, substantial corrections need to be taken into account. These corrections differ from standard ones because they depend on the specific procedure used for measuring the whole diffraction peak. To obtain the F^2_{hkl} values, the Lorentz (L), polarization (P), irradiated volume (V) and absorption (A) corrections must be applied to the integrated intensities, so that

$$F^2_{hkl} = I^{\rm M}_{hkl} L/(PVA), \tag{1}$$

with

$$L = \begin{cases} \Delta\omega(2\pi/\lambda)\sin 2\theta & \text{(for an } \omega \text{ scan)}, \\ \Delta\varphi(2\pi/\lambda)\sin 2\theta \sin\Psi & \text{(for a } \varphi \text{ scan)}, \end{cases} \tag{2}$$

$$P = (1 + \cos^2 2\theta)/2, \tag{3}$$

$$V = St/\sin\gamma, \tag{4}$$

$$A = \left\{\mu t\left[\frac{1}{\sin\gamma} + \frac{1}{\sin(2\theta - \gamma)}\right]\right\}^{-1} \times \left(1 - \exp\left\{-\mu t\left[\frac{1}{\sin\gamma} + \frac{1}{\sin(2\theta - \gamma)}\right]\right\}\right). \tag{5}$$

$\Delta\omega$ and $\Delta\varphi$ are the corresponding angles rotated along the scan, λ is the wavelength, t is the film thickness, S is the cross section of the incident beam in the direction normal to propagation, γ is the incident angle, and μ is the absorption coefficient. Table 1 lists the values of the integrated intensities and corrected structure factor amplitudes, to illustrate the relevance of these corrections. The derivation of these expressions, based on the kinematical theory of diffraction (the film was thinner than the extinction length), is detailed in Appendix *A*. The fact that in our experiments the primary beam is illuminating the entire sample thickness justifies the use of the kinematical approximation.

4. Application of δ recycling and refinement of the unit-cell contents

The structure was solved by δ recycling direct methods (Rius, 2012*a*) as implemented in *XLENS_v1* (Rius, 2012*b*). The fifth set of starting random phases yielded the true solution. The found relative scattering powers and (x/a, y/b, z/c) coordinates were (1000, $\frac{1}{4}$, $\frac{3}{4}$, $\frac{1}{2}$) for site 1 (2*b* Wyckoff position of *P*4/*nmm*, origin choice 2), (900, $\frac{3}{4}$, $\frac{3}{4}$, 0.231) for site 2 and (478, $\frac{3}{4}$, $\frac{3}{4}$, 0.823) for site 3 (2*c* Wyckoff positions). The respective scattering powers strongly suggest that site 1 is fully occupied by Cu, that As is at site 2 and that Mn partially occupies site 3. These results are consistent with independent structural and compositional information presented in §5.

The z coordinates of sites 2 and 3 together with their respective occupancies were refined with the single-crystal least-squares program *SHELXL97* (Sheldrick, 2008). We employed the following definitions for $wR2$, $R1$ and S: $wR2 = \{\sum[w(F_{\rm o}^2 - F_{\rm c}^2)^2]/\sum[w(F_{\rm o}^2)^2]\}^{1/2}$; $R1 = \sum ||F_{\rm o}| - |F_{\rm c}|| / \sum |F_{\rm o}|$; $S = \sum\{[w(F_{\rm o}^2 - F_{\rm c}^2)^2]/(n - p)\}^{1/2}$, with $w = 1/\sigma^2(F_{\rm o})$, where n is the number of reflections and p the number of refined parameters. The refinement converged to a residual $wR2$ = 0.1770 for 34 data and eight refined parameters; S = 0.643; $R1$ = 0.1112. The values of the z coordinates remained unchanged compared to the direct methods ones [0.236 (2), 0.841 (5), for sites 2 and 3, respectively] and the individual $U_{\rm eq}$ values were

Table 2
Structural details of the CuMnAs thin film.

The unit-cell parameters are a = 3.820 (10) Å and c = 6.318 (10) Å and the space group is $P4/nmm$ (No. 129). Cu mainly occupies Wyckoff position 2b ($\frac{1}{4}, \frac{3}{4}, \frac{1}{2}$), and Mn and As mainly occupy positions 2c ($\frac{3}{4}\ \frac{3}{4}\ z$). The Mn site is not fully occupied and the As site is partially replaced by Cu and Mn. All non-diagonal atomic displacement parameters are zero forced by site symmetry.

100% Cu		84% As; 8% Cu; 8% Mn			86% Mn		
$U_{11} = U_{22}$	U_{33}	z	$U_{11} = U_{22}$	U_{33}	z	$U_{11} = U_{22}$	U_{33}
0.025 (6)	0.085 (11)	0.2347 (13)	0.013 (4)	0.020 (5)	0.8298 (30)	0.016 (6)	0.038 (12)

all close to 0.02 Å^2. The refined occupancies for sites 2 (As) and 3 (Mn) are 0.964 (15) and 0.863 (13), respectively, so that the corresponding sum of electrons in the cell (the three sites) is 1 × 29 + 0.964 × 33 + 0.863 × 25 = 82.39. This sum, properly scaled, must be equal to the one derived from the atomic proportions measured experimentally. The actual composition of the thin films was obtained by variable voltage electron probe microanalysis, using a CAMECA SX-50 electron microprobe equipped with four wavelength-dispersive X-ray spectrometers. The results shown in Fig. 2(*a*) indicate the composition Cu 1.13 (2), As 0.88 (2), Mn 0.98 (2), which is constant over a distance of several millimetres, well above the beam width of 50 µm employed during the X-ray experiments. Hence, by making $k(1.13 \times 29 + 0.88 \times 33 + 0.98 \times 25) = 82.39$, it follows that k = 0.9546. After multiplying by k, the atomic content of the cell is 1.08 Cu, 0.84 As and 0.94 Mn. Since site 1 was assumed to be fully occupied by Cu and since from the refinement it is known that there are 0.86 Mn at site 3, this gives for site 2 the composition 0.84As + 0.08Cu + 0.08Mn. The sum is strictly 1.00 and we conclude that site 2 is essentially fully occupied. It must be highlighted that 0.964 As (the refined occupation) is nearly equivalent (in scattering power) to 0.84As + 0.08Cu + 0.08Mn (31.82 e$^-$ *versus* 32.04 e$^-$). In conclusion, the refinement converged to $wR2$ = 0.1066 and $R1$ = 0.0933 (nine parameters); S = 0.391. The final z coordinates for sites 2 and 3 and atomic displacement parameters are given in Table 2.[1]

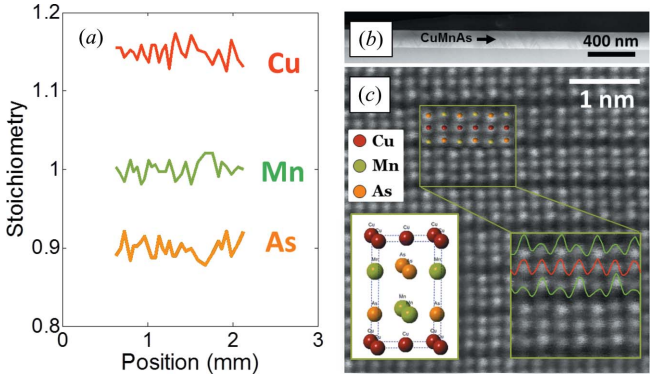

Figure 2
(*a*) Line profiles of the relative atomic composition on the same sample obtained by X-ray dispersive wavelength spectroscopy (*b*) Low-magnification *Z*-contrast image showing a flat and continuous layer over long lateral distances. The arrow points to the CuMnAs layer. (*c*) High-resolution *Z*-contrast image of the CuMnAs phase along the [100] direction obtained by aberration-corrected STEM. The inset, which is a higher magnification of the region marked with a green rectangle, shows the intensity profiles of the *Z*-contrast image along three different atomic planes. The sketch shows the CuMnAs structure.

5. Independent structural analyses

For atomic scale information on the structure, we used aberration-corrected STEM. The thin films were examined in a Nion UltraSTEM column, operated at 100 kV and equipped with a fifth-order Nion aberration corrector. Specimens for STEM observations were prepared by conventional thinning, grinding, dimpling and Ar ion milling. Figs. 2(*b*) and (*c*) show a low- and a high-magnification *Z*-contrast image of the CuMnAs thin film, respectively. High-resolution images of the interface region (not shown) proved that the interface is sharp, and that in-plane and out-of-plane textured growth occurs. In STEM, the high-angle annular dark field detector allows the recording of incoherent *Z*-contrast images in which the contrast of an atomic column is approximately proportional to the square of the average atomic number (Z). In this situation, heavier atomic columns can be easily distinguished from lighter ones, as shown in the figure inset, where the intensity profiles of the *Z*-contrast image along three different atomic planes emphasizes the contrast variation observed in every atomic column. Accordingly, atomic identities can be assigned on the basis of the model obtained from X-ray analyses and the image intensity. In agreement with the conclusions of the X-ray diffraction analyses, the atomic positions replicate the wiggling observed in sites 2 and 3 in tetragonal CuMnAs.

6. Conclusions

We have developed an experimental methodology that allows us to obtain a large set of structure factor moduli in thin films using laboratory X-ray equipment (Cu $K\alpha$ radiation). Using this methodology, we have solved and refined the average structure of a material prepared in the form of a thin film without prior knowledge of the film structure. In this case, substrate-induced stress stabilizes a tetragonal phase different from the bulk orthorhombic structure. We derived the expressions of the corrections necessary to transform the raw integrated intensities into a set of structure factor amplitudes suitable for the application of single-crystal direct methods. The structural model was derived by δ recycling, and the refined atomic positions and occupancies are in excellent agreement with an independent STEM and stoichiometry characterization. The present method has been successfully used to obtain bond distances and angles in oxide films as thin as 10 nm (Serrao *et al.*, 2013).

[1] Supplementary data are available from the IUCr electronic archives (Reference: RG5041). Services for accessing these data are described at the back of the journal.

APPENDIX A
Corrections to integrated intensities

The integrated intensities ($I^{\rm M}_{hkl}$) measured as explained above are not directly the square of the structure factor (F^2_{hkl}). In order to obtain F^2_{hkl} for the structural resolution and refinement, some corrections must be applied. This appendix specifies and explains the corrections that have been applied.

A1. Lorentz-equivalent correction

A diffraction peak is spread around its theoretical position in reciprocal space, mainly owing to its finite size, the strain of the sample and the divergence of the incident beam: $I(\mathbf{Q}) = I_{hkl}H(\mathbf{Q} - \mathbf{Q}_{hkl})$. In this expression, $I(\mathbf{Q})$ denotes the intensity at a general point $\mathbf{Q}$ of the reciprocal space, H is the corresponding spreading function (normalized $\int_{\mathbb{R}} H\,{\rm d}^3\mathbf{Q} = 1$) and I_{hkl} is the integrated intensity (corrected for geometrical factors). Thus, I_{hkl} could be obtained by the following integral in the three-dimensional reciprocal space:

$$I_{hkl} = \int\int_{V_Q}\int I(\mathbf{Q})\,{\rm d}^3\mathbf{Q}, \tag{6}$$

where V_Q is a suitable volume region around $\mathbf{Q}_{hkl}$ that must contain the whole diffraction peak.

In contrast, according to the data collection procedure described above, the measured integrated intensity is

$$I^{\rm M}_{hkl} = (1/T)\int_T {\rm d}t \int\int_A {\rm d}A\, I(\mathbf{Q}), \tag{7}$$

where T is the total measuring time; the first integral refers to the summation during the measurement (scan) and the double one to the summation over the area detector.

Thus, $I^{\rm M}_{hkl}$ and I_{hkl} are related by the path followed by the diffraction peak to cross the area detector (or, equivalently, the Ewald sphere) in the reciprocal space as a result of the film rotation (ω scan or φ scan) performed during data collection. More precisely, they are related by the volume element scanned by the detector for the time element, which can be expressed as ${\rm d}^3\mathbf{Q} = {\rm d}Q_\perp {\rm d}A = v_\perp\,{\rm d}t\,{\rm d}A$, where the subscript $\perp$ denotes the direction perpendicular to the area detector A and $v_\perp$ is the projection of the area-detector velocity, in reciprocal space, along this direction. This is illustrated for an ω scan in Fig. 3. The velocity of every point in the reciprocal space is given by the angular velocity used for the scan times the distance to the rotation axis. It must be mentioned that neither this distance nor the velocity is homogeneous for all the points covered by the detector, but the variations from point to point can be neglected (in the region where the peak appears). For an ω scan this velocity is given by $v_Q = \Omega Q \simeq \Omega Q_{hkl} = \Omega(4\pi\sin\theta/\lambda)$ (Ω is the angular velocity used for the scan) and its projection onto the perpendicular to the area detector is given by $v_\perp \simeq \Omega(4\pi\sin\theta/\lambda)\cos\theta = \Omega(2\pi/\lambda)\sin 2\theta$. This leads to

$$I_{hkl} = \Delta\omega I^{\rm M}_{hkl}(2\pi/\lambda)\sin 2\theta, \tag{8}$$

where $\Delta\omega$ is the total angle rotated along the ω scan ($\Delta\omega = \Omega\Delta T$).

For a non-specular reflection, as illustrated in Fig. 4, the distance to the rotation axis in reciprocal space is given by $Q\sin\Psi = (4\pi/\lambda)\sin\theta\sin\Psi$. Thus, the projection of the velocity along the direction perpendicular to the detector (along the diffracted beam) is given by $v_\perp \simeq \Omega(4\pi/\lambda)\sin\theta\sin\Psi\cos\theta = \Omega(2\pi/\lambda)\sin 2\theta\sin\Psi$. As for the ω scan, the velocity is not the same for all points on the detector, but the differences are small enough that this approximation is very reasonable. This expression leads to

$$I_{hkl} = \Delta\varphi I^{\rm M}_{hkl}(2\pi/\lambda)\sin 2\theta\sin\Psi, \tag{9}$$

where $\Delta\varphi$ is the angle rotated for the φ scan.

A2. Polarization correction

The integrated intensities are affected by the polarization of the beam. The correction (in the present case the primary beam is non-polarized) is given by the well known expression (*International Tables for Crystallography*, 2006)

$$I_{hkl} \propto F^2_{hkl}(1 + \cos^2 2\theta)/2. \tag{10}$$

We note that this expression is only appropriate for setups without primary beam polarizers. This is the case for our low-resolution setup, focusing on the collection of as many reflections as possible.

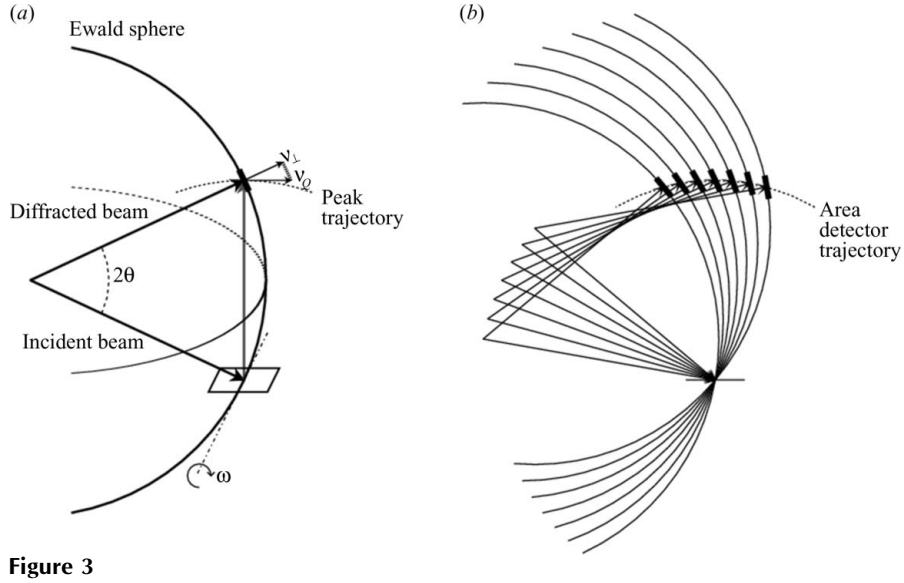

Figure 3
(*a*) Illustration of the reciprocal space crossing the Ewald sphere. Rotation of the film causes the rotation of the entire reciprocal space. In particular a diffraction peak will follow the dashed line and cross the Ewald sphere with a velocity v_Q given by Q times the angular velocity used to rotate the film. (*b*) Illustration of the process taking the reciprocal space (or the film) as the reference. In this case, the area detector 'travels' in reciprocal space and the volume scanned during this travel is summed into the measured integrated intensities.

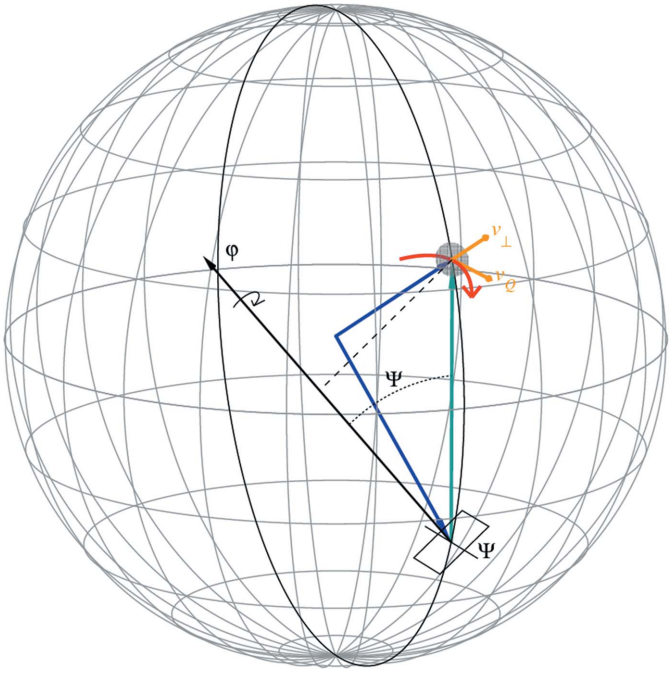

Figure 4
Representation of the Ewald sphere in which the film (square) is tilted along Ψ and rotated around the φ axis. Dark-blue arrows represent the incident and diffracted beam, the turquoise arrow is the **Q** point at the center of the detector, the black arrow shows the φ axis, the dashed straight line shows the turning radius, the red arrow shows the trajectory of the point at the center of the detector, and the orange arrows show the velocity of the **Q** point at the center of the detector (v_Q) and the component perpendicular to it ($v_\perp$).

A3. Irradiated volume correction

Since the sample is a thin film the irradiated volume varies with the angle between the sample and the incident beam (γ). The diffracted intensity is proportional to the irradiated volume, and this effect must be corrected with

$$I_{hkl} \propto F_{hkl}^2 V_{\rm irr} = F_{hkl}^2 St/\sin\gamma, \qquad (11)$$

where S and t are the incident beam cross section and the film thickness, respectively. This expression assumes that the size of the incident beam does not exceed that of the whole film. We have checked that this is fulfilled in the case presented in this work using coplanar geometry, but in the case of grazing-incidence geometries, this might not be true and this expression would have to be revised accordingly.

It must also be pointed out that, for specular reflections, the incident angle γ is equal to ω and thus it varies along the scan. Consequently, for this type of reflection, this correction would have to be applied during collection. Nonetheless, we can assume that for the small region (in reciprocal space) where the diffraction peak is located the variations will not be relevant and a constant γ can be employed.

A4. Absorption correction

This correction is required because the direct and diffracted beams are (partially) absorbed by the sample along their path. This absorption is different for every reflection. A beam diffracted at a depth x travels through the sample along a distance given by the expression $d = x[1/\sin\gamma + 1/\sin(2\theta-\gamma)]$. Taking this into account and integrating through the whole film, the final expression for the absorption correction is

$$I_{hkl} \propto F_{hkl}^2 \mu t \left[\frac{1}{\sin\gamma}+\frac{1}{\sin(2\theta-\gamma)}\right]^{-1} \times \left(1-\exp\left\{-\mu t\left[\frac{1}{\sin\gamma}+\frac{1}{\sin(2\theta-\gamma)}\right]\right\}\right), \qquad (12)$$

where μ is the absorption coefficient of the film and t is the film thickness. If the condition $\mu t << 1$ is satisfied this correction can be neglected.

All of the authors thank X. Llobet from the Scientific and Technological Center of the University of Barcelona for the chemical analysis. XM acknowledges the Czech Science Foundation (project P204/11/P339). JG acknowledges a JAE CSIC grant. Research at UCM (MAR) was supported by an ERC starting investigator award, grant No. 239739 STEMOX. The research was supported in part by ORNL's Shared Research Equipment (ShaRE) User Facility, which is sponsored by the Office of BES, US DOE. JR and CF acknowledge financial support from the Spanish Ministerio de Ciencia e Innovación Tecnológica (projects MAT2009-07967, consolider NANOSELECT CSD2007-00041) and the Generalitat de Catalunya. TJ and VN acknowledge support from the ERC Advanced Grant 268066-0MSPIN and from the Ministry of Education of the Czech Republic (grant No. LM2011026). CR acknowledges financial support from Fondazione Cariplo *via* the project EcoMag (project No. 2010-0584).

References

Ferrari, M. & Lutterotti, L. (1994). *J. Appl. Phys.* **76**, 7246–7255.
He, B. B. (2009). *Two Dimensional X-ray Diffraction*. New Jersey: John Wiley and Sons.
International Tables for Crystallography (2006). Vol. C, 1st online ed, ch. 6.2, pp. 596–598. Chester: International Union of Crystallography.
Máca, F., Mašek, J., Stelmakhovych, O., Martí, X., Reichlová, H., Uhlířová, K., Beran, P., Wadley, P., Novák, V. & Jungwirth, T. (2012). *J. Magn. Magn. Mater.* **324**, 1606–1612.
May, S. J., Kim, J.-W., Rondinelli, J. M., Karapetrova, E., Spaldin, N. A., Bhattacharya, A. & Ryan, P. J. (2010). *Phys. Rev. B*, **82**, 014110.
Mundelein, J. & Schuster, H. (1991). *Z. Naturforsch. Teil B*, **47**, 925–928.
Nateprov, A. N., Kravtsov, V. Ch., Fritsch, V. & von Loehneysen, H. (2011). *Surf. Eng. Appl. Electrochem.* **47**, 540–543.
Rius, J. (2012*a*). *Acta Cryst.* A**68**, 399–400.
Rius, J. (2012*b*). *XLENS_v1*, http://www.icmab.es/crystallography/software.
Serrao, C. R., Liu, J., Heron, J. T., Singh-Bhalla, G., Yadav, A., Suresha, S. J., Paull, R. J., Yi, D., Chu, J.-H., Trassin, M., Vishwanath, A., Arenholz, E., Frontera, C., Železný, J., Jungwirth, T., Marti, X. & Ramesh, R. (2013). *Phys. Rev. B*, **87**, 085121.
Sheldrick, G. M. (2008). *Acta Cryst.* A**64**, 112–122.
Wadley, P., Novak, V., Campion, R., Rinaldi, C., Marti, X., Reichlova, H., Zelezny, J., Maca, F., Masek, J., Holy, V., Edmonds, K. W., Gallagher, B. L., Foxon, C. T., Wunderlich, J. & Jungwirth, T. (2013). *Nat. Commun.* **4**, 2322.